Differential Mode Active EMI Filter Design for a Boost Power Factor Correction AC/DC Converter

Rajib Goswami, *Student Member, IEEE*, Shuo Wang, *Senior Member, IEEE*, Eugene Solodovnik, and Kamiar J. Karimi, *Member, IEEE*

***Abstract*— The objective of this paper is to introduce a methodology to design an active differential mode (DM) filter at the input side of ac/dc converters to cancel DM electromagnetic interference noise within concerned frequency range. The boost power factor correction ac/dc converter was taken as an example for DM active filter design. The active filter is analyzed based on the developed DM noise model. The design of DM active filter to achieve desired insertion gain and stability is addressed in detail. Both simulations and experiments were conducted to validate the proposed methodology. It is found that the proposed design methodology can meet the design objective and the stability challenge for the DM active filter of ac/dc converters.**

***Index Terms*— AC/DC converters, active differential mode (DM) electromagnetic interference (EMI) filter, boost power factor correction (PFC), DM noise.**

I. Introduction

ALMOST all of the switching-mode power conversion systems generate conducted electromagnetic interference (EMI) noise. The EMI can be categorized as differential mode (DM) and common-mode (CM) EMI. The noise flowing between the power conversion systems and ground is usually called CM noise and the noise flowing between power delivery paths is called DM noise. Passive *LC* filters are widely used in industry to attenuate EMI. However, the size, weight, and cost of the passive EMI filters are always a big concern for power electronics industry. Because filter inductors must carry full load current and DM capacitors must withstand full ac line voltages, the passive DM filters can be very big. Hybrid filters incorporating an active and a smaller passive filter have the potential to reduce the size of the passive DM EMI filters. Hence, thorough investigation of hybrid DM EMI filters is important.

Manuscript received November 6, 2017; revised January 28, 2018 and March 29, 2018; accepted April 27, 2018. Date of publication May 23, 2018; date of current version February 11, 2019. This work was supported in part by the Boeing Company and in part by National Science Foundation under Grant 1540118. Recommended for publication by Associate Editor Wuhua Li. *(Corresponding author: Shuo Wang.)*

R. Goswami is with the Electrical and Computer Engineering Department, University of Texas at San Antonio, San Antonio, TX 78249 USA (e-mail: rajibshohag@gmail.com).

S. Wang is with the Electrical and Computer Engineering Department, University of Florida, Gainesville, FL 32611 USA (e-mail: shuowang@ieee.org).

E. Solodovnik and K. J. Karimi are with Boeing Company, Seattle, WA 98124 USA (e-mail: eugene.v.solodovnik@boeing.com; kamiar.j.karimi@boeing.com).

Color versions of one or more of the figures in this paper are available online at http://ieeexplore.ieee.org.

Digital Object Identifier 10.1109/JESTPE.2018.2839734

To reduce the EMI filter size, weight, and cost hybrid CM EMI filters have been proposed in [1]–[17]. In a hybrid CM filter, an active filter attenuates the low-frequency (LF) CM noise and a passive filter attenuates the high-frequency (HF) CM noise. Because the corner frequency of the passive filter is significantly increased, the CM EMI filter size could be significantly reduced. However, an EMI filter is composed of a CM and a DM functional unit. The hybrid CM filter can only reduce the size and weight of the CM functional unit. To further reduce the size of the whole system, the size and weight of the DM functional unit must be reduced. Most of the existing techniques address the CM active filter [1]–[17]. Some literatures address the issues of DM active filter design for dc/dc applications [18]–[20]. On the other hand, the DM active filter design for ac/dc converters is deemed to be very challenging [21] and there are few papers to address this topic [21], [22].

There are big differences in CM and DM active filter design in case of ac/dc converters. In a DM active filter, while sensing the DM noise voltage/current, the power line frequency voltage/current is included along with DM EMI noise in the sensed signal [21], [22]. This is different in case of CM active filter, as CM noise sensing part cancels all the DM signals including the power line frequency voltage/current and DM EMI noise and senses CM noise only [1]. Hence, unlike CM active filter, DM active filter for ac/dc converters must have a high-pass filter (HPF) to reject the power line frequency voltage/current. However, it is also difficult to maintain a very low gain at the power line frequency and a high gain at the beginning of the EMI frequency range, as there are only a few decades distance between these frequencies and hence, there must be a sharp rise in the gain of the active filter which introduces stability issues [21]. For example, when the switching frequency is low, the topology and control technique used in [21] could not solve the stability issue while trying to maintain substantial mid-band gain, as well as sufficiently low gain at the frequencies of the power line current. There are also HF stability issues associated with the amplifier's HF poles, which needs to be compensated. Until now, a good hybrid DM active filter design which analyzes and solves all the different issues associated with stability and hardware design including detailed mathematical modeling is not found in the available literature.

In this paper, the DM noise model of an ac/dc boost power factor correction (PFC) converter and the EMI

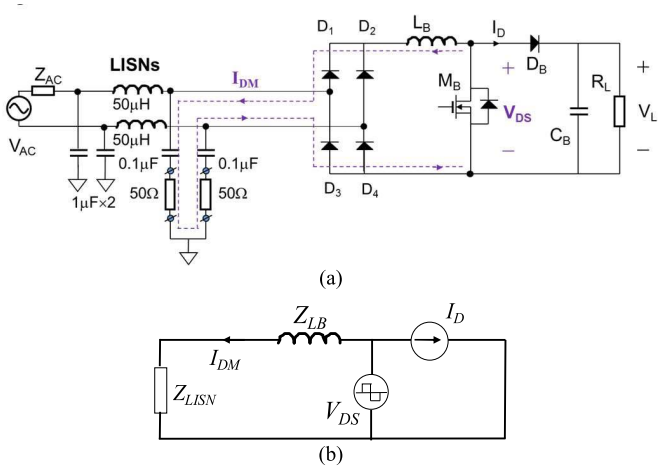

Fig. 1. DM noise in a boost PFC ac/dc converter. (a) DM noise. (b) DM noise model.

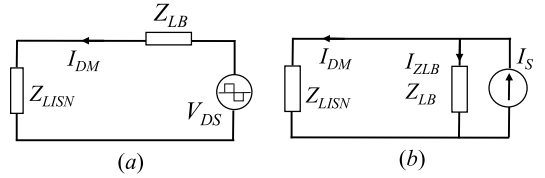

Fig. 2. DM noise model of the boost PFC converter. (a) Thevenin equivalent circuit. (b) Norton equivalent circuit.

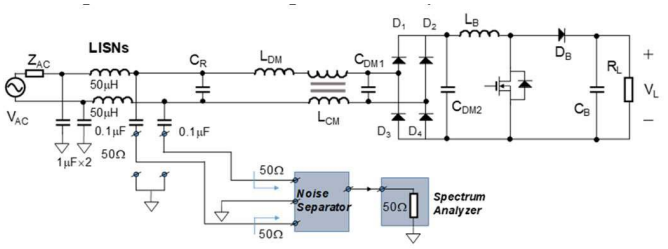

Fig. 3. EMI noise measurement setup for a commercial boost PFC converter with a passive EMI filter.

attenuation requirement for the active filter is first discussed. The active filter's design methodology is then explored in detail. The developed design methodology includes the design and modeling at component level, active filter level and system level. The closed-loop model is derived based on a feedback control scheme for an ac/dc system with a hybrid EMI filter. The system's stability is analyzed and compensation is proposed to achieve stability based on the derived loop gain. Both simulation and experiments validated the developed design methodology. The designed active DM EMI filter in this paper ensures a low gain at the power line frequency and has a high gain at the EMI frequency while maintaining the stability at both LF and HF. Hence, with the proposed hybrid DM EMI filter, the overall passive DM filter's size is significantly reduced. These are important improvements over available papers in the DM EMI filter design for ac/dc converters.

II. DM Noise of a Boost PFC AC/DC Converter and Attenuation Requirement for Active EMI Filters

A. DM Noise Model

Boost PFC ac/dc converters have been widely used as front-end converters to improve grid power factor. A boost converter works at switching mode so it generates DM and CM noise. Fig. 1(a) shows a commercial boost PFC converter circuit with line impedance stabilization networks (LISNs) connected between the power line and the converter for EMI measurement. The switching frequency of the PFC converter is 120 kHz. It has a 120-V ac input and 380-V dc ouput, and delivers 350-W power. The path of DM noise current $I_{\rm DM}$ is shown in Fig. 1(a).

Based on the substitution theory, the DM noise model of the converter can be developed by replacing the MOSFET, M_B with a voltage source which has the same voltage waveform as the drain to source voltage $V_{\rm DS}$, and by replacing the diode D_B, with a current source which has the same current waveform as the diode current I_D [29]. The impedances of C_B can be ignored as it is very small within the concerned EMI frequency range. The converter works at continuous conduction mode so diodes rectifier D_1–D_4 always conducts current due to the PFC operating status, and they can be considered as a short circuit. The impedance $Z_{\rm LISN}$ of LISNs is the load of DM EMI noise. If the LISNs are not present, the grid impedance will be the load impedance of the DM noise. If the impedance of the boot inductor L_B is $Z_{\rm LB}$, the DM noise model can be developed in Fig. 1(b).

Based on Fig. 1(b), the DM noise generated by $V_{\rm DS}$ and I_D can be analyzed based on superposition theory. It is found that I_D does not contribute to the DM noise on the ac input side because the voltage source $V_{\rm DS}$, which is treated as a short circuit when the effect of I_D is considered, shorts the I_D. Because current source I_D is treated as an open circuit when the effect of $V_{\rm DS}$ is considered, there is no DM noise current flowing through R_L, so it can be ignored. As a result, only $V_{\rm DS}$ generates DM noise as the Thevenin equivalence represented in Fig. 2(a). For the prototype used in this paper, the impedance of L_B is 324-μH inductance with HF parasitics. The Thevenin equivalence can be converted to a Norton equivalence in Fig. 2(b) for current gain derivation in Section III. Here, $I_S = V_{\rm DS}/Z_{\rm LB}$, and $I_{\rm ZLB}$ is the current flowing through the equivalent noise source impedance $Z_{\rm LB}$.

B. Passive DM EMI Filter

To meet the EMI standards in the input of the boost PFC converter, a large passive filter is usually used. In Fig. 3, a preexisting passive filter is used to meet CISPR-22 in this commercial product. The detailed passive filter design is out of the scope of this paper as it has been discussed extensively in [23]–[26]. In this filter, $C_{\rm DM2}$ and $C_{\rm DM1}$ are two DM filter capacitors. Both are 0.47 μF. $L_{\rm CM}$ is a coupled CM inductor with a value of 5 mH. It has a leakage inductance $L_{\rm DMCM} = 23.6$ μH for DM noise reduction. $L_{\rm DM}$ is a DM inductor with a value of 141 μH. C_R is a DM capacitor with

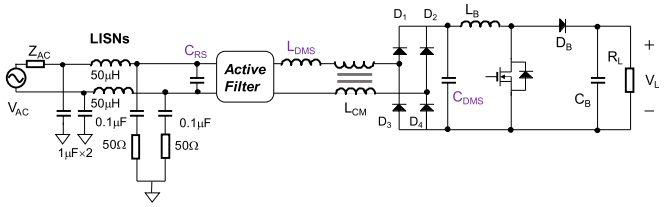

Fig. 4. Hybrid DM EMI filter with an active and a smaller passive filter.

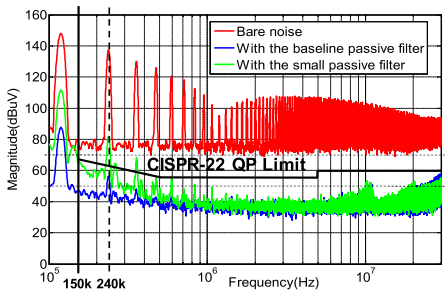

Fig. 5. DM noise spectra with and without passive filters.

a value of 0.47 μF. In Fig. 3, the EMI is measured through LISNs using a noise separator [28] and a spectrum analyzer.

C. Hybrid DM EMI Filter

Because the active filter can reduce LF DM noise, the pre-existing passive filter in Fig. 3 can be reduced to a smaller passive filter consisting of C_{RS}, L_{DMS}, L_{CM}, and C_{DMS} in Fig. 4. The two DM capacitors C_{DM1} and C_{DM2} in Fig. 3 are functionally parallel. Hence, they are reduced to a single smaller capacitor C_{DMS} in Fig. 4. The hybrid EMI filter consists of this small passive filter and an active filter. In Fig. 4, the active filter is placed between the filter inductor L_{DMS} and capacitor C_{RS} to meet the high source impedance and low load impedance requirement as described in [1]. The choice of the values of the smaller passive filter components in relation to the active filter gain is described in Section II-D.

D. EMI Attenuation Requirement for the Active Filter

In the hybrid filter, if a high gain can be achieved by the active filter at the beginning of the EMI frequency range, the remaining attenuation requirement can be achieved by the small passive filter, so that the hybrid filter meets the overall attenuation requirement. But, for the DM active filter, the maximum attenuation is limited by stability constraints at both the LF and HF crossovers, as discussed in Section I. Now, reducing the attenuation requirement for the passive filter means its corner frequency can be increased by reducing the values of the inductor and capacitors. It has been shown in [27] that the passive DM EMI filter (*LC* filter) volume is exponentially decreased with the decrease in attenuation requirement, which means a small reduction in the attenuation requirement from the passive filter can significantly reduce the passive filter size. In this design, at first, the values of the passive filter components should be chosen so that the passive filter size can be greatly reduced, and the remaining attenuation can be provided by the active filter while maintaining stability through compensation. Even after compensation, if it is not possible to provide the remaining attenuation by the active filter while maintaining stability, the component values of the passive filter need to be increased to meet the overall requirement.

In this design, the component values of the baseline DM filter components have been reduced by more than half, so that the hybrid filter size could be reduced by more than half. From Fig. 4, as C_{RS} is paralleled with LISN, the noise voltage drop on LISN is determined by C_{RS} instead of LISN. Also, because C_{DMS} is in parallel with the rest of filter and L_B is in series with the filter, L_B forms a low-pass filter with C_{DMS} and the rest of the filter. Because $L_B >> L_{\mathrm{DMS}}$ and L_{DMCM}, the first corner frequency is given by, $f_{c1} \approx (1/(2\pi(L_B \times (C_{\mathrm{DMS}} + C_{\mathrm{RS}})))^2)$ [24]. Similarly, the second corner frequency, f_{c2} can be determined by network theory and is related to L_{DMS}, L_{DMCM}, and C_{RS}. To increase/decrease the attenuation of the passive filter at the desired frequency, these two corner frequencies, f_{c1} and f_{c2} need to be decreased/increased, respectively. Based on this, the values of L_{DMS}, C_{DMS}, and C_{RS} can be adjusted.

For the small passive filter, at first the value of the DM inductor, L_{DMS} is chosen. It cannot be too small as the active filter needs high input impedance (shall be discussed later). The value of L_{DMS} is chosen to be the half of L_{DM}, hence, $L_{\mathrm{DMS}} = 71$ μH. The value of the other two components is chosen so that they are smaller than half in value of the baseline filter's capacitors. They are, $C_{\mathrm{DMS}} = 0.22$ μF, $C_{\mathrm{RS}} = 0.22$ μF. L_{DMCM} is not changed as it is the leakage inductance of the CM inductor. Next, the attenuation requirement of the active filter can be determined based on this small passive filter's attenuation.

In order to derive the required EMI attenuation for the active filter, bare DM noise from the converter without any EMI filter applied was first measured at full load 350 W. The noise measurement setup is similar to that in Fig. 1(a). In the second step, the DM noise spectrum with the preexisting baseline passive filter, as shown in Fig. 3, was measured. Finally, without the active filter, the DM noise spectrum with only the small passive filter in Fig. 4 was measured. The spectrum analyzer used in these experiments is a Tektronix RSA306.

In Fig. 5, based on the measured EMI spectra and the CISPR-22 EMI standard, the active filter's attenuation requirement can be determined. For the bare noise, the converter's second order switching harmonic at 240 kHz is the highest harmonic that falls inside the conducted EMI frequency range 150 kHz–30 MHz. To meet the standard, the total attenuation A_{TOT} of the small passive filter and the active filter should be $(137 - 62 + 6)$ dB $= 81$ dB, where 6 dB is the attenuation margin. Of this total attenuation requirement, 55 dB is attenuated by the small passive filter and the remaining 26 dB needs to be attenuated by the active filter.

III. Active DM EMI Filter Design

The active filter should meet several requirements: first, it should achieve the desired noise attenuation; second,

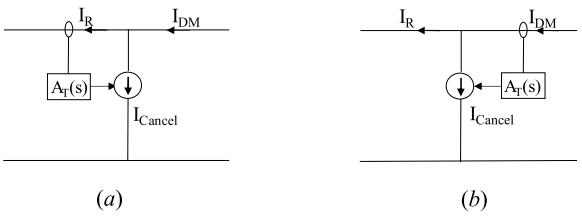

Fig. 6. Control schemes. (a) Feedback. (b) Feedforward.

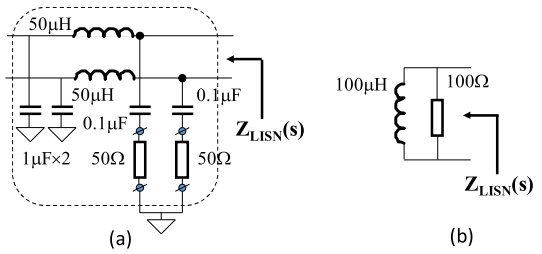

Fig. 7. Equivalent impedance model of LISNs for DM noise. (a) Circuit of LISNs. (b) Equivalent impedance of LISNs.

it should work stably; third, it should have low power loss; and fourth, the active filter should be small and light.

A. Noise Sensing and Cancellation

Based on noise sensing and noise cancellation method, active EMI filters can be of four different topologies: 1) voltage sensing—voltage injection; 2) current sensing (CS)—voltage injection; 3) voltage sensing—current injection; and 4) CS—current injection.

For the active filter using voltage injection method, a voltage transformer is needed in series with ac power line. It must therefore carry full converter power currents. Furthermore, the transformer magnetizing inductance must be big enough to reduce the magnetizing current supplied from the active filter to reduce the power loss of the active filter. Because of this, the transformer is big and heavy which contradicts active filter's objective: filter size and weight reduction. Hence, voltage injection is avoided in this paper.

For the DM noise sensing, a current transformer (CT) is a simple way to directly sense DM noise current. With a proper CT structure, it is also possible to easily eliminate the influence of CM noise current which can complicate the active filter design. By properly selecting a turn ratio and a load resistance, the transfer resistance of the CT can be easily higher than 1 Ω, for example 3 Ω, which is good to achieve high loop gain and wide bandwidth for the active filter. On the other hand, the DM noise voltage on power lines can also be sensed. However, the sensed voltage includes not only the DM noise voltage but also 50/60 Hz line voltage which is much bigger than DM noise voltage. A voltage divider and a high order HPF will be needed to reduce voltage level and remove the sensed 50/60 Hz voltage. This reduces the gain of voltage sensing and requires the amplifier in the active filter has a high gain to compensate the low gain of voltage sensing. This in turn reduces the bandwidth of the active filter due to a fixed gain-bandwidth product. Furthermore, high voltage rating components may also be needed in voltage sensing, this will limit the volume reduction too. Based on the analysis above, CS—current injection (CSCI) will be used for the active filter design in this paper.

B. Active Filter Control Schemes

Based on the control scheme, a CSCI active filter can be designed in two ways: 1) feedback and 2) feedforward. These two configurations are shown in Fig. 6. $I_{\rm DM}$ is the DM noise current from the noise source. I_R is the noise current flowing through the LISNs or grid after the active filter is inserted.

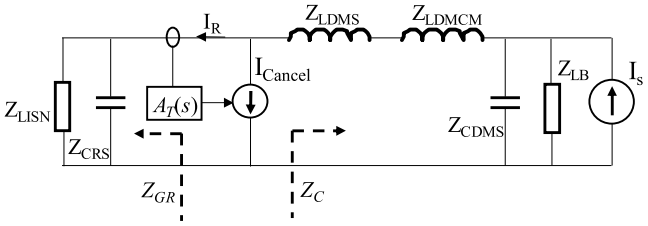

Fig. 8. CSCI feedback active filter topology with the source and load impedances.

$I_{\rm Cancel}$ is the cancellation current injected by the active filter. $A_T(s)$ is the current gain of the active filter.

For feedback control, the active filter's gain $A_T(s)$ should be big and with wide bandwidth. For feedforward control, to achieve a good cancellation, the active filter's gain $A_T(s)$ should be as close to unity as possible. It has a strict requirement on the values of key components. Feedforward control does not improve the unity-gain bandwidth of the active filter over feedback control due to the fixed unity-gain bandwidth of a given operational amplifier. Its improvement in the noise attenuation at the passband is very much dependent on the accuracy of the component values used in the design [1]. Due to the flexibility of the feedback control, it is selected in this paper.

C. DM Noise Model With Active Filter

A typical circuit of LISNs is shown in Fig. 7(a). Within the concerned frequency range from 150 kHz to 30 MHz, the impedance of 0.1- and 1-μF capacitors can be ignored, so the DM impedance of LISNs in Figs. 1, 3, 4, and 6 can be approximately modeled as a resistance $R_{\rm LISN} = 100\ \Omega$ in parallel with an inductance $L_{\rm LISN} = 100\ \mu$H, as shown in Fig. 7(b).

In Fig. 4, with the reduced passive EMI filter, the system's DM noise model, including the model of CSCI active filter with feedback control, the DM noise model of the ac/dc boost PFC converter and the DM model of LISNs, can be derived in Fig. 8. In Fig. 8, I_R is the noise current flowing through the active filter's equivalent load impedance $Z_{\rm GR} = Z_{\rm CRS}||Z_{\rm LISN}$. The Norton equivalent impedance of the DM noise source including the passive filter and the ac/dc converter is $Z_C = Z_{\rm LDMS} + Z_{\rm LDMCM} + Z_{\rm CDMS}||Z_{\rm LB}$.

In Fig. 8, the output of the active filter can be represented with its Thevenin equivalent circuit as shown in Fig. 9. In Fig. 9, $V_{\rm out}$ and $Z_{\rm out}$ are Thevenin equivalent output voltage

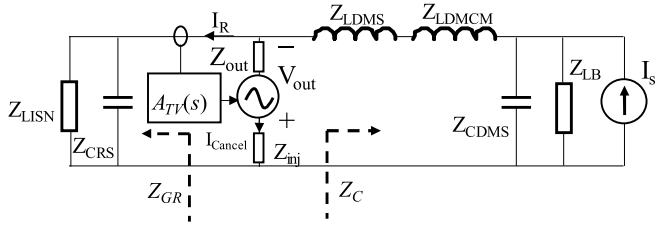

Fig. 9. CSCI feedback active filter topology implemented with an amplifier and an injection network.

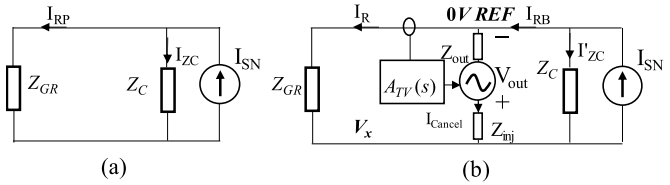

Fig. 10. Norton equivalent noise models of the boost PFC converter. (a) Without active filter. (b) With the active filter.

and impedance of the active filter. $A_{\rm TV}(s)$ is active filter's transfer-impedance and $A_{\rm TV}(s) = V_{\rm out}/I_R$. The impedance of the injection network is $Z_{\rm inj}$.

D. Active Filter Insertion Gain

Based on Fig. 9, the DM noise models without and with the active filter are shown in Fig. 10(a) and (b). In Fig. 10

$$I_{\rm SN} = I_S \times \frac{Z_{\rm CDMS}||Z_{\rm LB}}{Z_{\rm LDMS} + Z_{\rm LDMCM} + Z_{\rm CDMS}||Z_{\rm LB}}$$

is the Norton equivalent noise current source. In Fig. 10(a), $I_{\rm RP}$ is the current flowing through $Z_{\rm GR}$ and $I_{\rm ZC}$ is the current flowing through the Norton equivalent impedance Z_C. In Fig. 10(b), after the insertion of active filter, I_R is the current flowing through $Z_{\rm GR}$; $I_{\rm RB}$ is the current before the active filter's current injection node (0-V reference) on the top line and $\rm I'_{ZC}$ is the current flowing through the Norton equivalent impedance Z_C. V_x is the voltage on the other line.

Based on Fig. 10(a), the current gain $G_{\rm OL}(s)$ from $I_{\rm SN}$ to $I_{\rm RP}$ without the active filter can be derived as

$$G_{\rm OL}(s) = \frac{I_{\rm RP}(s)}{I_{\rm SN}(s)} = \frac{Z_C}{Z_C + Z_{\rm GR}}. \tag{1}$$

After the insertion of the active filter in Fig. 10(b), it is found that, $(I_{\rm SN}(s) - I_{\rm Cancel}(s)) \times G_{\rm OL}(s) = I_R(s)$ and $V_x = -I_R(s) \times Z_{\rm GR}$. Based on this, $I_{\rm Cancel}$ can be derived as follows:

$$I_{\rm Cancel}(s) = \frac{I_R(s) \times A_{\rm TV}(s) + I_R(s) \times Z_{\rm GR}}{Z_{\rm out} + Z_{\rm inj}}. \tag{2}$$

The closed-loop signal flow diagram for the model of Fig. 10(b) can be derived based on these equations as shown in Fig. 11.

Based on the signal flow diagram, the current gain $G_{\rm CL}(s)$ with the active filter can be derived as follows:

$$G_{\rm CL}(s) = \frac{I_R(s)}{I_{\rm SN}(s)} = \frac{G_{\rm OL}(s)}{1 + G_{\rm OL}(s) \times \frac{A_{\rm TV}(s)+Z_{\rm GR}}{Z_{\rm out}+Z_{\rm inj}}}. \tag{3}$$

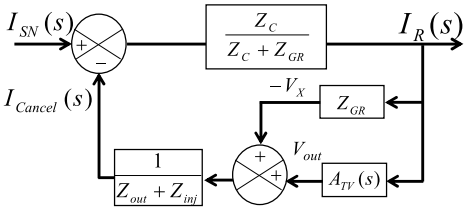

Fig. 11. Closed-loop signal flow diagram of the CSCI FB active filter.

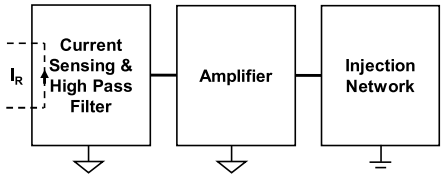

Fig. 12. Active filter circuit block.

The insertion gain $G_{\rm IS}(s)$, which is defined as the ratio of the current flowing through $Z_{\rm GR}$ with the active filter in Fig. 10(b) to that without the active filter in Fig. 10(a), can be derived as

$$\begin{aligned} G_{\rm IS}(s) &= \frac{G_{\rm CL}(s)}{G_{\rm OL}(s)} = \frac{I_R(s)}{I_{\rm RP}(s)} = \frac{1}{G_{\rm OL}(s)} \\ &\quad \times \frac{G_{\rm OL}(s)}{1 + G_{\rm OL}(s) \times \frac{A_{\rm TV}(s)+Z_{\rm GR}}{Z_{\rm out}+Z_{\rm inj}}} \\ &= \frac{1}{1 + G_{\rm OL}(s) \times \frac{A_{\rm TV}(s)+Z_{\rm GR}}{Z_{\rm out}+Z_{\rm inj}}}. \end{aligned} \tag{4}$$

$G_{\rm IS}(s)$ should be as small as possible. Because of this, active filter's gain $A_{\rm TV}(s)$ should be big and with enough bandwidth. $G_{\rm OL}(s)$ should be also as close to unity as possible to achieve small $G_{\rm IS}(s)$. It means source impedance Z_C should be much larger than load impedance $Z_{\rm GR}$.

In Fig. 9, in the 150 kHz–30 MHz frequency range, $Z_{\rm CDMS}||Z_{\rm LB}$ is mostly determined by the capacitors impedance $Z_{\rm CDMS}$ and it is much smaller than $Z_{\rm LDMS} + Z_{\rm LDMCM}$, therefore, Z_C is mostly determined by $Z_{\rm LDMS} + Z_{\rm LDMCM}$. Moreover, in Fig. 4, because DM capacitor $C_{\rm RS}$ is located between the active filter and the power grid/LISNs to meet the impedance requirements above, $Z_{\rm GR}$ is mostly determined by the $Z_{\rm CRS}$. Therefore, the source and load impedances meet the condition, $Z_C >> Z_{\rm GR}$.

E. Filter Architecture

The circuit block of the active filter in Fig. 10(b) is shown in Fig. 12. In Fig. 12, the CSCI active filter consists of CS and HPF function block, amplifier block and injection network block.

The CS and HPF function block consists of a CT and a second-order HPF to sense current and reject undesired LF current below the concerned EMI frequency range. The amplifier block includes a preamplifier and a current amplifier to have enough current injection capability. The current injection network consists of an injection capacitor $C_{\rm inj}$ in series with an injection resistor $R_{\rm inj}$. It isolates the active filter from the other high-voltage ac line, works as a HPF and stabilizes its impedance at high frequencies.

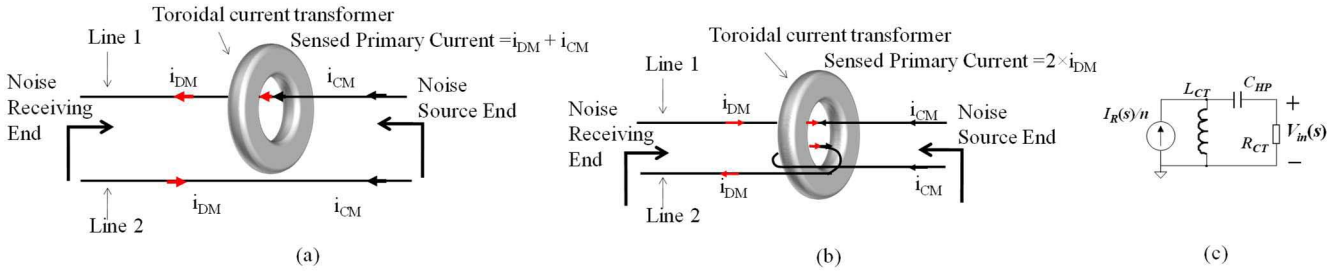

Fig. 13. CS and HPF. (a) Conventional CS method. (b) DM CS with CM current injection. (c) Model of CT with an HPF.

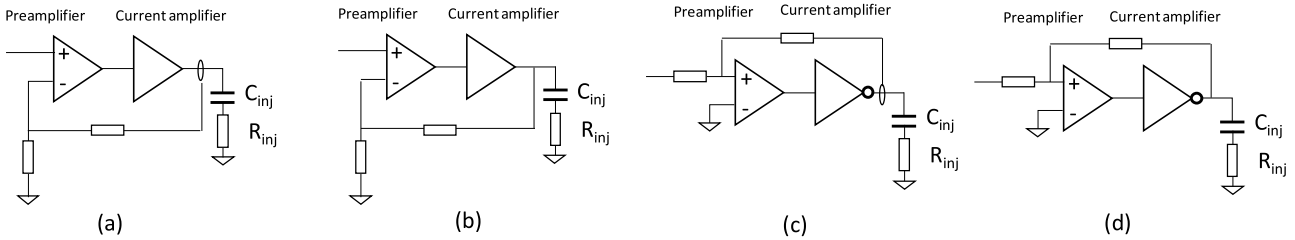

Fig. 14. Amplifier configuration. (a) Current series feedback. (b) Voltage series feedback. (c) Current parallel feedback. (d) Voltage parallel feedback.

F. Design of CT and HPF

1) DM Noise Current Sensing: The ac/dc converter also generates CM noise which flows between the power line and the ground. Conventional CT CS method is shown in Fig. 13(a). CT senses both the CM and DM currents. If the DM cancellation current is injected based on the sensed CM current, the mixed mode noise current will be generated. It will complicate the noise reduction so the sensed CM current should be rejected. The CM current can be simply rejected in CT with the sensing method in Fig. 13(b).

In Fig. 13(b), ac line 1 conducts current $i_{DM}+i_{CM}$ and ac line 2 conducts current $-i_{DM}+i_{CM}$. the ac line 1 goes through the CT's toroidal core so current $i_{DM}+i_{CM}$ generates magnetic flux inside the core. The ac line 2 also passes through the core but in the reverse direction so that i_{DM}–i_{CM} generate magnetic flux inside the core. As a result, the magnetic flux generated by i_{CM} is canceled and the magnetic flux generated by i_{DM} is doubled. Compared with conventional CS in Fig. 13(a), the advantage of this DM CS method is: 1) it rejects undesired CM noise and 2) the CT's gain is increased by 6 dB.

2) Current Transformer Integrated With a High-Pass Filter: A toroidal CT with a turn ratio 1:n is designed to sense the DM current with the technique in Fig 13(b). The magnetizing inductance of the secondary is L_{CT}. The sensed current includes both EMI noise component and line frequency current component.

One of the biggest differences between the active filters of an ac/dc converter and a dc/dc converter is the active filter of an ac/dc converter should avoid injecting line frequency current because the line frequency current is not the noise current and it usually has large magnitude as it carries the power of the ac/dc converter. Because of this, HPF should attenuate line frequency current as well as its harmonics in the sensed current to ensure that the active filter has a small power loss due to the undesired LF current injection below the EMI frequency range. The sensed EMI current below the concerned frequency range should also be rejected to reduce power loss if possible.

In Fig. 13(c), C_{HP} is added between CT inductance L_{CT} and its load resistance R_{CT}. L_{CT}, C_{HP}, and R_{CT} is a HPF with an I–V transfer function. If the input impedance of the amplifier block is very high, the CT's I–V transfer function is therefore:

$$\frac{V_{in}(s)}{I_R(s)}=\frac{2\times\left(\frac{s}{\omega_c}\right)^2\frac{R_{CT}}{n}}{1+\frac{s}{\omega_c Q}+\left(\frac{s}{\omega_c}\right)^2} \tag{5}$$

where

$$\omega_c=\frac{1}{\sqrt{L_{CT}C_{HP}}}$$

and

$$Q=\frac{1}{R_{CT}}\sqrt{\frac{L_{CT}}{C_{HP}}}.$$

The HPF introduces phase shift which may cause stability issues for the active filter at the crossover frequencies. Hence, ω_c must be appropriately selected so the HPF has sufficient phase and gain margin at the crossover frequencies and enough attenuation to line frequency current components.

G. Design of Amplifier

1) Amplifier Feedback Configurations: The amplifier block of Fig. 12 could be implemented with either current series feedback, voltage series feedback, current parallel feedback, and voltage parallel feedback configuration, and they are shown in Fig. 14 with the injection network connected.

The amplifier of Fig. 14(a) is a current series feedback amplifier which regulates the output current and has a high input impedance. The amplifier in Fig. 14(b) is a voltage series

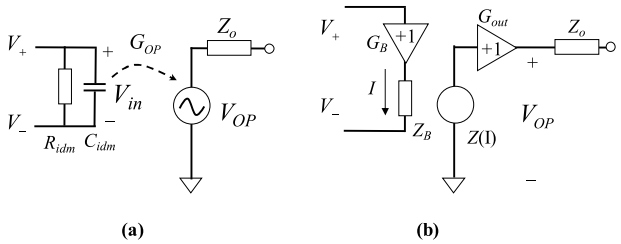

Fig. 15. Open-loop OPAM equivalent circuit. (a) VFA. (b) CFA.

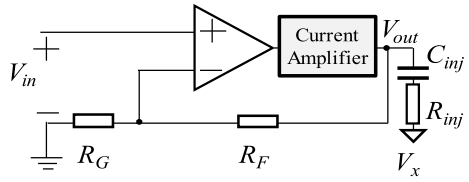

Fig. 16. Amplifier circuit configuration.

feedback amplifier which regulates the output voltage and has a high input impedance. The amplifier in Fig. 14(c) is a current parallel feedback amplifier which regulates the output current and has a limited input impedance. The amplifier in Fig. 14(d) is a voltage parallel feedback amplifier which regulates the output voltage and has a limited input impedance. The output voltage of the current feedback amplifier in Fig. 14(a) and (c) may have a dc offset issue due to the unbalanced charge on the capacitor C_{inj} in the injection network or load impedance. The charge on the capacitor will build up and may finally saturate the output and then the active filter cannot work properly. The dc offsets also reduces the range of output voltage. The voltage feedback amplifier in Fig. 14(b) and (d) regulates the output voltage, so there is no output dc offset issue. In order to reduce amplifier input impedance's influence to the gain and corner frequency of CS and HPF block, instead of using parallel feedback amplifier, the voltage feedback amplifier should be used. Although voltage feedback amplifier is used, it can still inject cancellation currents as the output voltage is added to the injection network and the load impedance. Based on the analysis above, a voltage series feedback configuration is selected for the amplifier.

2) Number of Preamplifier Stages: Multistage preamplifiers can increase the open-loop gain of the amplifier. It leads to an increased −3-dB bandwidth. However, the open-loop gain of an operational amplifier usually has a single pole within the concerned frequency range. As a result, one stage preamplifier introduces $-\pi/2$ phase shift and m stage cascaded preamplifiers introduce $-\text{m}\pi/2$ phase shift. With more than one stage preamplifiers, the $A_T(s)$ will have more phase shift which will easily cause stability issues. As a comparison, CT almost has no phase shift within the concerned frequency range. Because of this, a single stage preamplifier is preferred.

3) Preamplifier Circuit Configurations: A operational amplifier (OPAM) will be used in the preamplifier. OPAMs are generally of two types: 1) voltage feedback OPAM (VFA) and 2) current feedback OPAM (CFA). The open-loop equivalent circuits of VFA and CFA are shown in Fig. 15. G_{OP} is the open-loop gain of the VFA and R_{idm}, C_{idm}, and Z_{o} are the input resistance, the input capacitance, and the output impedance, respectively. $V+$ and $V-$ are the input voltages in the two input pins and V_{OP} is the open-loop output voltage of the amplifier. For CFA, $Z(I)$ is the transimpedance gain, G_B and G_{out} are unity gain buffers, Z_{o} is the output impedance and Z_B is the small input impedance in the inverting pin.

For a VFA, its gain-bandwidth product is constant, so when gain increases, the bandwidth will decrease. For a CFA, its bandwidth is independent of its gain, so it can achieve a wider bandwidth than a VFA [32], [33]. However, for the EMI with a small passive filter in Fig. 5, LF EMI is a major concern, so a very wide bandwidth is not the first priority in the selection of OPAM.

For the amplifier with a voltage series feedback is shown in Fig. 16, the feedback resistance R_F will be designed and compensated based on the stability and the desired loop gain profile of the whole system which includes the active filter, the passive filter, the converter and LISNs. However, for a CFA, the value of R_F strongly influences the stability and the bandwidth of the OPAM [32], [33], so it has a limited range to choose from and cannot be chosen freely. Furthermore, CFA has output offset issue which is not desired as discussed in Section III-G.1. On the other hand, the R_F design for a VFA is simpler than a CFA as its value can be selected in a wide range without stability issues. The compensation can also be easily added to R_F to achieve the desired loop gain and stability for the whole system without compromising the stability of the OPAM as shown in Sections IV and V.

Because of the reasons above, a VFA is selected in this paper for the active filter design. It does not mean CFA is not a good choice for the active filter design. When a wide bandwidth is a major concern, a CFA could be considered if there is no stability issue. In this paper, a VFA, AD829 is chosen which has a wide unity-gain bandwidth of 120 MHz and high rail-to-rail voltage (±15 V) which is good for high output voltage swing.

4) Current Amplifier Design: A class AB amplifier is used in the output stage of the active filter to achieve higher current injection capacity. A typical configuration is shown In Fig. 17.

The n-p-n and p-n-p transistors should have high bandwidth so they do not reduce the active filter's bandwidth for the specified EMI frequency range. They should have enough current injection capacity and have sufficient power ratings. ZDT6753, an n-p-n–p-n-p complementary pair was chosen in the design. The two transistors in ZDT6753 have very similar features. It has a typical transition frequency (bandwidth) of 175 MHz and hence does not have adverse effects in the concerned EMI frequency range. Diodes D1 and D2 set the bias voltage for two transistors. The design of biasing circuit including the design of biasing current, biasing diodes and biasing resistance $R_{\text{B1,2}} = R'_B$ has been discussed in detail in [1] so it will not be repeated here.

The emitter resistors R_{E1} and R_{E2} are used to solve thermal runaway issue. In Fig. 17, the voltage drop of the two biasing diodes is determined by characteristics of the diodes. Based on the I_{BE}–V_{BE} characteristics of the transistors, the base current I_{BE} increases when the transistor temperature increases due to conduction power loss. This causes the transistors to enter linear region. As a result, there is more current flowing through

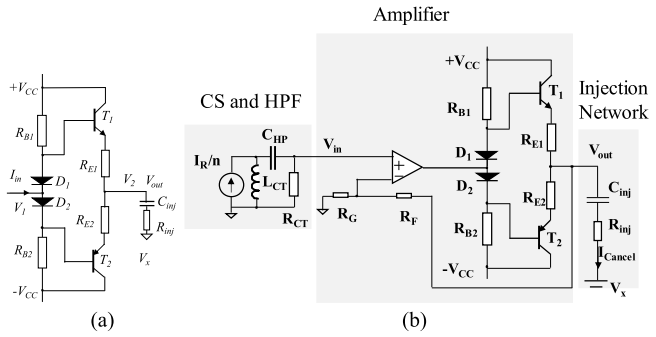

Fig. 17. (a) Class AB amplifier with thermal runaway solution. (b) Final active filter circuit.

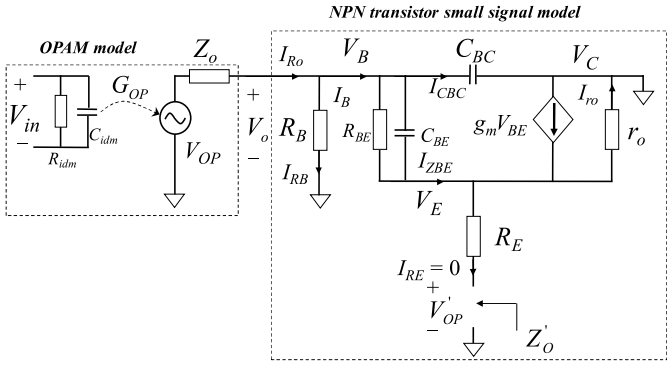

Fig. 18. Open-loop small signal equivalent circuit of the amplifier block.

two transistors and generating high conduction power loss. This in turn further increases the device temperature until the transistors are killed.

$R_{\rm E1}$ and $R_{\rm E2}$ provide a negative feedback to stabilize the BE junction bias voltage. In the experiments, they were proved to be a very efficient solution to thermal runaway issue. $R_{\rm E1} = R_{\rm E2} = R_E$ can be designed based on

$$R_E = \frac{V_T \ln \frac{I_D I_S}{I_C I_{\rm SD}}}{I_C} \tag{6}$$

where V_T is the thermal voltage, I_D is the diode current, $I_{\rm SD}$ is the diode saturation current, I_C is the collector current, and I_S is the BE junction saturation current. The actual R_E used is 5 Ω which is smaller than the calculated 11 Ω through (6).

5) Transfer Function of the Amplifier: The final active filter circuit is shown in Fig. 17 (b). The open-loop small signal model of the amplifier without injection network connected is shown in Fig. 18. Because transistor pair ZDT6753 has a symmetric model structure and only one transistor conducts current at the same time, only one transistor model is shown in Fig. 18. In Fig. 18, the OPAM equivalent circuit is the same as in Fig. 15(a) for a VFA. Based on AD829's datasheet [30], the open-loop output impedance Z_0 can be derived and found to be approximately 20 Ω [34]. The value of open-loop dc gain $G_{\rm O}$ as a function of load can also be found from the datasheet. In Fig. 18, V_B, V_E, and V_C are base, emitter, and collector voltages, respectively. $R_B = R_{\rm B1} || \ R_{\rm B2} = R'_B/2$. $R_{\rm BE}$ is base to emitter resistance. $C_{\rm BE}$ is the base to emitter capacitance. $C_{\rm BC}$ is the base to collector capacitance. $r_{\rm o}$ is the output resistance of the transistor. g_m is the transconductance. The transistor's current gain $\beta = g_m Z_{\rm BE}$. Z'_O is the open-loop output impedance of the whole open-loop amplifier, and $V'_{\rm OP}$ is the open-loop output voltage. The transistor's model parameters can be procured from the datasheet and the extraction through measurements under the dc bias of $V_{\rm CC} = 15$ V with $R_B = R_{\rm B1} || R_{\rm B2} = 2.3$ kΩ and $R_E = 5$ Ω. The procured parameters are $C_{\rm BC} = 30$ pF, $C_{\rm BE} = 300$ pF, $R_{\rm BE} = 469$ Ω, $r_{\rm o} = 20.3$ kΩ, $g_m = 0.32$, and $\beta = 150$.

Based on Fig. 18, the open-loop voltage gain $G_{\rm OPC}$ from $V_{\rm in}$ to $V'_{\rm OP}$ can be derived as

$$G_{\rm OPC} = \frac{V'_{\rm OP}}{V_{\rm in}} = \frac{K_P \times G_{\rm o}}{\left(1 + \frac{s}{\omega_{\rm OP1}}\right)\left(1 + \frac{s}{\omega_{\rm OP2}}\right)\left(1 + \frac{s}{\omega'_{\rm PBC}}\right)}. \tag{7}$$

In (7), the poles $\omega_{\rm OP1}$ and $\omega_{\rm OP2}$ are OPAM's open-loop poles which can be derived from its datasheet. The frequencies of these two poles are,

$$f_{\rm OP1} = \frac{1}{2\pi\,\omega_{\rm OP1}} = 10 \text{ kHz}$$

and

$$f_{\rm OP2} = \frac{1}{2\pi\,\omega_{\rm OP2}} = 35 \text{ MHz}.$$

The pole $\omega'_{\rm PBC}$ is generated by the class AB amplifier.

In (8)

$$K_P = \frac{R_P}{Z_o + R_P}, \quad \omega'_{\rm PBC} = \omega_{\rm PBC} \times \left(1 + \frac{R_P}{Z_o}\right)$$
$$\omega_{\rm PBC} = \frac{1}{C_{\rm BC} \times R_P}$$

and

$$\frac{1}{R_P} = \frac{1}{r_o\,(\beta + 1)} + \frac{1}{R_B}.$$

Z'_O can be derived as

$$Z'_O = R_E + \frac{(Z_{Z_o C_{\rm BC}} + Z_{\rm BE}) \times r_o}{(\beta + 1) \times r_o + Z_{Z_o C_{\rm BC}} + Z_{\rm BE}} \tag{8}$$

where $Z_{Z_o C_{\rm BC}} = Z_o || R_B || (1/sC_{\rm BC})$ and $Z_{\rm BE} = R_{\rm BE} || (1/sC_{\rm BE})$. Because $(Z_{Z_o C_{\rm BC}} + Z_{\rm BE}) << r_0$, Z'_O can be approximately calculated as

$$Z'_O \approx R_E + \frac{(R_o + R_{\rm BE})}{(\beta + 1)} \approx 8.2\Omega.$$

Based on (7), the closed-loop voltage gain $A_{\rm VA}$ from $V_{\rm in}$ to $V_{\rm out}$ in Fig. 17(b) when the injection network is not connected can be derived as

$$A_{\rm VA} = \frac{V_{\rm out}}{V_{\rm in}} = \frac{\frac{G_{\rm OPC}}{Z'_o}}{\frac{1}{Z'_o} + \frac{1}{R_G + R_F} + \frac{R_G}{R_G + R_F} \times \frac{G_{\rm OPC}}{Z'_o}}. \tag{9}$$

From Fig. 22, the Thevenin equivalent output impedance, $Z_{\rm out}$ of the amplifier block can be derived as [31]

$$Z_{\rm out} = \frac{Z'_o}{\left(1 + \left(\frac{R_G}{R_G + R_F}\right) G_{\rm OPC}\right)}. \tag{10}$$

H. Design of Current Injection Network

The current injection network in Fig. 17(b) consists of an injection capacitor C_{inj} in series with a small resistor R_{inj}. The injection network has three functions: 1) C_{inj} is needed for the isolation of the active filter from high-voltage ac line; 2) C_{inj} and R_{inj} also generate a first order high-pass filter to further reduce the undesired injection currents at the frequencies below the specified frequency range in EMI standards; and 3) R_{inj} limits the injection current spikes and stabilizes HF impedance.

The load impedance of the class AB amplifier is the impedance of the injection network in series with the impedance between two power lines: $Z_{\text{GR}}||Z_C$, as shown in Figs 9 and 10. Hence, load impedance, $Z_{\text{load}} = Z_{\text{inj}} + Z_{\text{GR}}||Z_C$. Due to the small impedance of C_{RS} in Z_{GR} within the concerned frequency range, the load impedance of the class AB amplifier is mostly determined by the injection network if the injection network is properly designed. Hence, $Z_{\text{load}} \approx Z_{\text{inj}} = R_{\text{inj}} + (1/sC_{\text{inj}})$ and the injected cancellation current I_{Cancel}

$$I_{\text{Cancel}} \approx \frac{V_{\text{out}}}{Z_{\text{inj}}} = \frac{V_{\text{out}} \times sC_{\text{inj}}}{1 + \frac{s}{\omega_{\text{inj}}}} \tag{11}$$

where $\omega_{\text{inj}} = 1/(R_{\text{inj}}C_{\text{inj}})$. Due to the zero at the origin in (11), the current I_{Cancel} increases as frequency increases up to the corner frequency ω_{inj}. Z_{inj} will be capacitive until ω_{inj}. The capacitive Z_{inj} introduces $-90°$ phase shift which can cause stability issue which will be discussed later. In EMI spectrum, because the highest DM noise spikes are usually at low frequencies as shown in Fig. 5, the I_{Cancel} should be maximized close to the first DM noise spike at the beginning of the concerned frequency range. ω_{inj} should therefore be close to the first DM noise spike so the maximum injection current gain can be achieved for the highest DM noise spike. Moreover, R_{inj} introduces power loss and reduces current gain at HFs, so it should not be too large. C_{inj} can therefore be found based on ω_{inj} and R_{inj}.

I. Active Filter Transfer Function

Based on the derived transfer functions for the CS-HPF block and amplifier block, from Fig. 17(b), the transfer function from the sensed noise current I_R to the Thevenin equivalent output voltage V_{out} of the active filter can be derived as follows:

$$\begin{aligned} A_{\text{TV}}(s) &= \frac{V_{\text{out}}(s)}{I_R(s)} = \frac{V_{\text{in}}(s)}{I_R(s)} \times \frac{V_{\text{out}}(s)}{V_{\text{in}}(s)} = \frac{V_{\text{in}}(s)}{I_R(s)} \times A_{\text{VA}}(s) \\ &= \frac{2 \times \left(\frac{s}{\omega_{\text{HP}}}\right)^2 \frac{R_{\text{CT}}}{n}}{1 + \frac{s}{\omega_{\text{HP}}Q} + \left(\frac{s}{\omega_{\text{HP}}}\right)^2} \times \frac{\frac{G_{\text{OPC}}}{Z_o'}}{\frac{1}{Z_o'} + \frac{1}{R_G+R_F} + \frac{R_G}{R_G+R_F} \times \frac{G_{\text{OPC}}}{Z_o'}}. \end{aligned} \tag{12}$$

$A_{\text{TV}}(s)$, Z_{out}, Z_{inj}, Z_C, and Z_{GR} have been derived in this section. Based on the signal flow diagram of Fig. 11, the loop gain of the active filter can be derived, so active filter's stability can be analyzed and the compensation can be designed to ensure stability.

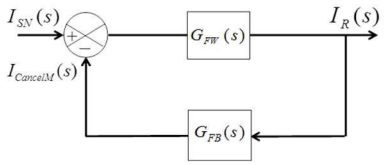

Fig. 19. Simplified signal flow diagram.

IV. Active Filter Stability Analysis and Compensation

A. Loop Gain of the Active Filter

In Fig. 11, to derive the loop gain of the active filter, one of the feedback paths $Z_{\text{GR}}/(Z_{\text{out}} + Z_{\text{inj}})$ should be combined with the forward path because it is due to the circuit connection instead of the action of the active filter. Based on the derivations in Section III, Fig. 11 can be simplified to Fig. 19. $I_{\text{CancelM}}(s)$ is an intermediate signal used in the derivation.

In Fig. 19, forward gain $G_{\text{FW}}(s)$ and feedback gain $G_{\text{FB}}(s)$ are

$$G_{\text{FW}}(s) = \frac{\frac{Z_C}{Z_C+Z_{\text{GR}}}}{1 + \frac{Z_C}{Z_C+Z_{\text{GR}}} \times \frac{Z_{\text{GR}}}{Z_{\text{out}}+Z_{\text{inj}}}} \tag{13}$$

$$G_{\text{FB}}(s) = \frac{A_{\text{TV}}}{Z_{\text{out}} + Z_{\text{inj}}}. \tag{14}$$

The loop gain $T_{\text{FB}}(s)$ can be derived by multiplying the forward path gain and feedback path gain as

$$T_{\text{FB}}(s) = \frac{\frac{Z_C}{Z_C+Z_{\text{GR}}}}{1 + \frac{Z_C}{Z_C+Z_{\text{GR}}} \times \frac{Z_{\text{GR}}}{Z_{\text{out}}+Z_{\text{inj}}}} \times \frac{A_{\text{TV}}(s)}{Z_{\text{out}} + Z_{\text{inj}}}. \tag{15}$$

B. Loop Gain Measurement and Stability

To validate the loop gain predicted by (15), the S-parameters S_{11}, S_{12}, S_{21}, and S_{22} were measured using a network analyzer, Copper Mountain Planar 808/1, and converted to loop gain using the method described in [23]. The measurement was conducted by breaking the feedback loop between the output of HPF (port 2) and the input of amplifier (port 1) and using voltage injection method shown in Fig. 20. V_1 is the injected signal to Port 1 from the network analyzer and the response from Port 2 was measured by the network analyzer. During the loop gain measurement, based on the superposition theory, the ac/dc converter was connected and the MOSFET M_B was shorted but the ac power was shut OFF, so the noise source I_S can be removed as shown in Fig. 20.

For the parameters of CT and HPF, $L_{\text{CT}} = 0.23$ mH, $C_{\text{HP}} = 10\ \mu$F, and $R_{\text{CT}} = 30\ \Omega$. The corner frequency of HPF is $f_c = (\omega_c/2\pi) = (1/2\pi\sqrt{L_{\text{CT}}C_{\text{HP}}}) \approx 3.36$ kHz. The CT was made with a J material toroidal core from Magnetic company. The characteristics of the core will be discussed in Section V for size comparison. For the amplifier, $R_G = 100\ \Omega$, $R_F = 1000\ \Omega$, R_{B1} and R_{B2} are 4.7 kΩ, and the biasing diodes D_1 and D_2 are 1N4148 high speed signal diodes. Both $R_{\text{E1}}$and R_{E2} are 5-Ω resistors. The value of injection capacitor, $C_{\text{inj}} = 0.2\ \mu$F and the injection resistor, $R_{\text{inj}} = 2.5\ \Omega$, with a corner frequency, $f_{\text{inj}} = (\omega_{\text{inj}}/2\pi) = (1/2\pi C_{\text{inj}}R_{\text{inj}}) \approx 318$ kHz. For

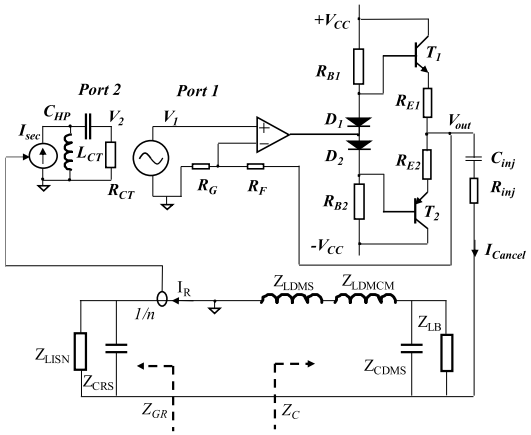

Fig. 20. Loop Gain measurement with voltage injection by breaking the feedback loop.

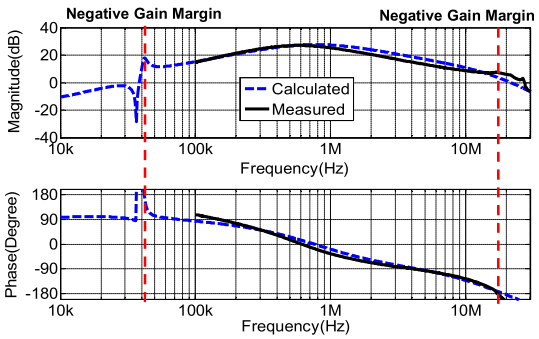

Fig. 21. Comparison of measured and calculated loop gains for the uncompensated active filter (unstable scenario).

the converter, the measured DM inductor impedance Z_{LDMS} is, $L_{\mathrm{DMS}} = 71\ \mu$H, with parasitic resistance, $R_{\mathrm{LDMS}} = 5.42\ \mathrm{k}\Omega$, and parasitic capacitance, $C_{\mathrm{LDMS}} = 6.1$ pF in parallel. The measured DM impedance, Z_{LDMCM} of the CM inductor is, $L_{\mathrm{DMCM}} = 23.6\ \mu$H, with parasitic resistance, $R_{\mathrm{LDMCM}} = 3\ \mathrm{k}\Omega$, and parasitic capacitance, $C_{\mathrm{LDMCM}} = 0.28$ nF in parallel. The impedance of the boost inductor, Z_B is $L_B = 327\ \mu$H, with parasitic resistance, $R_{\mathrm{LB}} = 2.97\ \mathrm{k}\Omega$, and parasitic capacitance, $C_{\mathrm{LB}} = 9.44$ nF in parallel. The two passive capacitors are, $C_{\mathrm{DMS}} = 0.2\ \mu$F and $C_{\mathrm{RS}} = 0.2\ \mu$F. They have very small parasitic inductance and resistance. LISN's impedance was described before.

In Fig. 21, the measured loop gain is compared with the one calculated using (15). They match well from 100 kHz to 30 MHz. Because the lowest frequency which the network analyzer can measure is 100 kHz, the measured loop gain is from 100 kHz to 30 MHz while the calculated loop gain is from 10 kHz to 30 MHz. In Fig. 21, there are two unstable frequency ranges, the first one is between 30 and 50 kHz and the other one is between 10 and 20 MHz. They should be compensated to achieve stability.

C. Analysis of Instability and Compensation Design (Below 100 kHz)

In Fig. 20, Z_{CDMS} and $Z_{\mathrm{LB}}$are in parallel. The corner frequency of the boost inductor, $L_B = 324\ \mu$H and DM capacitor, $C_{\mathrm{DMS}} = 0.22\ \mu$F is around 19 kHz. Hence, for the

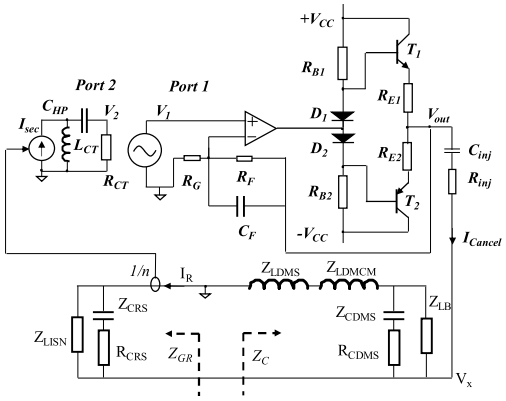

Fig. 22. Loop gain measurement setup with LF damping and HF compensation.

30 to 50 kHz frequency range, $Z_{\mathrm{CDMS}}||Z_{\mathrm{LB}}$ is approximately determined by the capacitors impedance Z_{CDMS}. In the grid side, Z_{GR} is approximately determined by the small impedance of the capacitor Z_{CRS}. In the active filter, the CS-HPF block's corner frequency f_c is much lower and the injection network's pole frequency f_{inj} is much higher than this frequency range. The amplifier's closed loop poles, which will be discussed later, inside A_{TV} are also at much higher frequencies than this frequency range. Hence, in this frequency range, $T_{\mathrm{FB}}(s)$ can be approximated as

$$T_{\mathrm{FB}}(s) = A_{\mathrm{TV}}(s) \times \frac{sC_{\mathrm{RS}}}{(K_C+1)} \times \frac{1+\left(\frac{s}{\omega_{\mathrm{DM}}}\right)^2}{1+\left(\frac{s}{\omega_{\mathrm{GOLP}}}\right)^2} \tag{16}$$

where $K_C = (C_{\mathrm{RS}} + C_{\mathrm{DMS}}/C_{\mathrm{inj}})$, the double zero is at

$$f_{\mathrm{DM}} = \frac{\omega_{\mathrm{DM}}}{2\pi} = \frac{1}{2\pi\sqrt{(L_{\mathrm{DMS}}+L_{\mathrm{DMCM}})\,C_{\mathrm{DMS}}}} \approx 36.5\ \mathrm{kHz} \tag{17}$$

and double pole is

$$f_{\mathrm{GOLP}} = \frac{\omega_{\mathrm{GOLP}}}{2\pi} = \frac{\sqrt{(K_C+1)}\omega_{\mathrm{DM}}\omega_{\mathrm{DMCR}}}{2\pi\sqrt{\left(K_C\omega_{\mathrm{DM}}^2+\omega_{\mathrm{DMCR}}^2\right)}} \tag{18}$$

where

$$\omega_{\mathrm{DMCR}} = \frac{1}{\sqrt{(L_{\mathrm{DMS}}+L_{\mathrm{DMCM}}) \times (C_{\mathrm{DMS}}||C_{\mathrm{RS}})}}$$

so $f_{\mathrm{GOLP}} \approx 44.4$ kHz. In (17), the two undamped resonances at f_{DM} and f_{GOLP}, caused by $L_{\mathrm{DMS}} + L_{\mathrm{DMCM}}$, C_{DMS}, and C_{RS} introduce a stability issue from 30 to 50 kHz in Fig. 26. To damp these resonances, a resistor $R_{\mathrm{CDMS}} = 5\ \Omega$ is added to be in series with C_{DMS}, and a resistor $R_{\mathrm{CRS}} = 1\ \Omega$ is added to be in series with C_{RS}, as shown in Fig. 22. As C_{DMS} is present in both ω_{DM} and ω_{GOLP}, in (16), R_{CDMS} can damp both the double poles and double zeros.

D. Analysis of Instability and Compensation Design (Above 100 kHz)

The amplifier's gain $A_{\mathrm{VA}}(s)$ in (9) is a factor of active filter transfer function $A_{\mathrm{TV}}(s)$ in (12). $A_{\mathrm{TV}}(s)$ is a factor of the

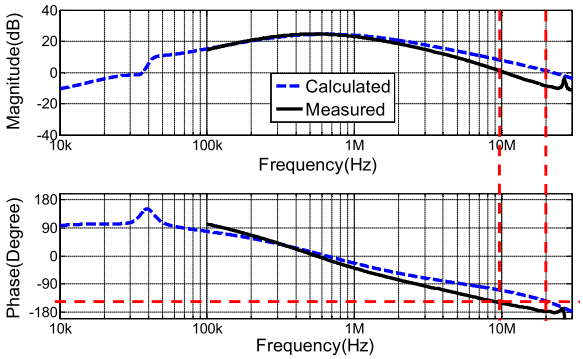

Fig. 23. Comparison of measured and calculated loop gain after damping and compensation.

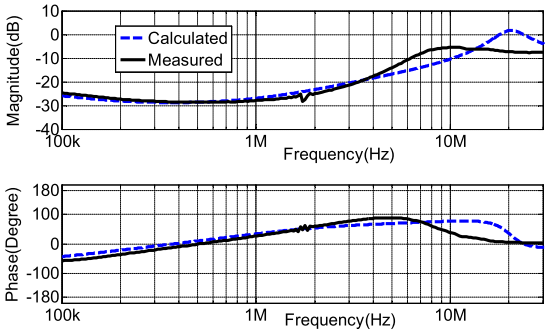

Fig. 24. Comparison of measured and calculated insertion gain for the compensated stable active filter.

loop gain $T_{\mathrm{FB}}(s)$ in (12). Because of this, $A_{\mathrm{VA}}(s)$ strongly influences the stability of the system. By compensating $i_{\mathrm{VA}}(s)$, the loop gain can be compensated. Based on (7) and (8), ignoring poles or zeros above 30 MHz beyond the concerned frequency range, the $A_{\mathrm{VA}}(s)$ in (9) can be approximately simplified to (19)

$$A_{\mathrm{VA}} \approx \frac{A_{\mathrm{NI}}}{1+\frac{s}{Q\omega_{\mathrm{UC}}}+\left(\frac{s}{\omega_{\mathrm{UC}}}\right)^2} \tag{19}$$

where

$$\omega_{\mathrm{UC}}=\sqrt{\frac{G_o\omega_{\mathrm{OP1}}\omega_{\mathrm{OP2}}}{A_{\mathrm{NI}}}},\quad Q\omega_{\mathrm{UC}}=\frac{G_o\omega_{\mathrm{OP1}}}{A_{\mathrm{NI}}}$$

and the noninverting amplifier gain $A_{\mathrm{NI}}=1+(R_F/R_G)$. With the parameters in this paper, $f_{\mathrm{UC}}=(\omega_{\mathrm{UC}}/2\pi)\approx 15$ MHz. This double pole introduces an abrupt $-180°$ change. Because there are parasitic poles which are not included in (19) above 30 MHz from the amplifier, the phase margin of the loop gain is negative at the crossover frequency in Fig. 21. If this double pole is split to two far-away separate single poles, the phase will change slowly across several decades, and enough phase margin could be achieved.

By paralleling a small capacitor C_F with the feedback resistor R_F as shown in Fig. 22, the double pole can be split to two separate single poles. A_{VA} can now be approximately represented as

$$A_{\mathrm{VA}} \approx \frac{A_{\mathrm{NI}}\left(1+\frac{s}{\omega_{\mathrm{CZ}}}\right)}{(1+\frac{s}{\omega_{\mathrm{CP1}}})(1+\frac{s}{\omega_{\mathrm{CP2}}})(1+\frac{s}{\omega_{\mathrm{CP3}}})} \tag{20}$$

where

$$\omega_{\mathrm{CZ}}=\omega_{\mathrm{PF}}A_{\mathrm{NI}},\quad \omega_{\mathrm{PF}}=\frac{1}{R_FC_F}$$

$$\omega_{\mathrm{CP1}}=\frac{1}{\frac{A_{\mathrm{NI}}}{G_o\omega_{\mathrm{OP1}}}+\frac{1}{\omega_{\mathrm{PF}}}},\quad \omega_{\mathrm{CP2}}=\omega_{\mathrm{OP2}}\left(1+\frac{G_o\omega_{\mathrm{OP1}}}{A_{\mathrm{NI}}\omega_{\mathrm{PF}}}\right).$$

ω_{CP3} is very close to ω_{CZ} so they cancel each other. With $C_F=30$ pF, the double pole is split to,

$$f_{\mathrm{CP1}}=\frac{\omega_{\mathrm{CP1}}}{2\pi}\approx 2.9\mathrm{MHz}$$

and

$$f_{\mathrm{CP2}}=\frac{\omega_{\mathrm{CP2}}}{2\pi}\approx 74\mathrm{MHz}.$$

The calculated and measured loop gains after damping and A_{VA} compensation are shown in Fig. 23. In Fig. 23, the stability is achieved in both LF and HF range with at least 40° phase margin.

It should be pointed out that, from the loop gains in Figs. 21 and 23, the loop gains have stability issues without compensation. After compensation they just have sufficient phase margins. If the loop gain is increased further, the stability of the active filter may not be maintained even with heavy compensation. Hence, the gain of the active filter was designed not only to reduce the passive filter size by half but also to have the maximum stable gain at both LF and HF.

V. Experimental Results

A. Insertion Gain Measurement and Comparison

After the damping and compensation, the insertion gain of the active filter was measured based on the method in [23]. The insertion gain of the active filter is defined as the ratio of the noise voltage on LISNs with to that without the active filter. The S-parameters of the active filter is measured with the Z_{GR} and Z_C in Fig. 10(b) replaced with the two ports of the network analyzer based on 50-Ω source and 50-Ω load impedance. Then based on Fig. 10(b), the measured S-parameters were converted to insertion gain with the noise source impedance Z_C and load impedance Z_{GR} [23]. In Fig. 24, the measured and calculated insertion gains based on (4) are compared. They match well below 10 MHz and have small difference between 10 and 30 MHz. It should be pointed out that the insertion gain is defined as the ratio of the current flowing through Z_{GR} with the active filter to that without the active filter and it is different from transfer gain, so the phase in Fig. 24 has no physical meaning for the active filter. The phase curves are compared in Fig. 24 for validation purpose only. Also, because the DM active filter injects the cancellation currents between two ac lines which are balanced by the DM capacitors, the CM noise will not be influenced by the DM active filter as the CM noise flows between two power lines and the ground.

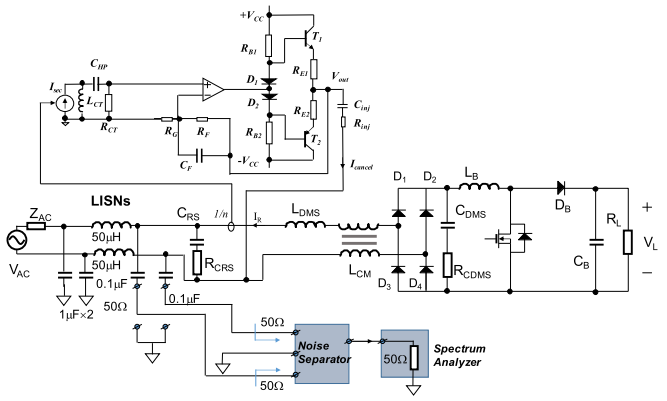

Fig. 25. DM noise spectrum Measurement with ac source, ac/dc converter, and a hybrid EMI filter.

B. EMI Spectrum Measurements With the AC/DC Boost Power Factor Correction Converter

The DM noise measurement setup is shown on Fig. 25 with a Boost PFC converter as a noise source. A DM noise separator [28] is connected to the output of the LISNs for DM noise measurement. The spectrum analyzer used in the experiment is a Tektronix RSA306. The switching frequency of the PFC converter is 120 kHz with a 120-V ac input and 380-V dc ouput. The compensation design and the calculated insertion gain will be validated via experiments. The EMI measurement results will show the designed active filter can meet the CISPR-22 standard.

To validate the identified unstable scenarios of Fig. 21, in the first experiment, the damping resistors, $R_{\rm CRS}$ and $R_{\rm CDMS}$ and the compensation capacitor C_F, are not used and the DM noise spectra without and with the active filter is shown in Fig. 26(a). Second, $R_{\rm CRS}$, $R_{\rm CDMS}$, and C_F were added back and the DM noise spectrum was measured and shown in Fig. 26(b). The load is 150 W in both cases to validate the predicted stability. In Fig. 26(a), there is a small bump in the LF range around 30–50 kHz and a big bump in the HF range between 10 and 20 MHz as predicted by the loop gain in Fig. 21. In Fig. 26, the noise reduction is also much less than that expected from the insertion gain of Fig. 24 because the active filter is not functioning properly due to instability. Whereas, after damping and compensation, in the measured spectrum of Fig. 26(b), the noise bumps are eliminated and the active filter achieved the expected attenuation as predicted by the insertion gain in Fig. 24.

Finally, the load of boost PFC converter was increased to 350 W. The bare EMI noise without any passive or active filters, the EMI with a baseline passive filter and the EMI with a small passive filter were measured in Fig. 5. The baseline filter can meet the EMI standard CISPR-22 quasi-peak (QP) limit. In this measurement, the EMI with the small passive filter and the active filter (hybrid filter) was measured and compared within Fig. 27. In Fig. 27(a), the hybrid filter can meet the CISPR-22 QP limit with the passive filter reduced by half from the baseline filter. In Fig. 27(a), with the small passive filter, several low-order switching harmonics are over the limit. With the hybrid filter all the EMI harmonics are within the limit and it also has the desired EMI reduction margin at 240 kHz as designed. A comparison between the EMI with baseline passive filter and hybrid filter was made in Fig. 27(b). In Fig. 27(b), the hybrid filter performance is as good as the big baseline passive filter. It is shown in Figs. 26 and 27 that the active filter's compensation and attenuation work well at both 150 W and 350 W load conditions. From Figs. 26 and 27, the 120-kHz switching noise is always dominant no matter with or without the active filter because 120 kHz is outside of the concerned frequency range and not supposed to be significantly reduced by the active filter. Because of this, no matter with or without the active filter, the noise currents flowing through the LISNs are always dominant by high 60-Hz line current and 120-kHz switching noise current.

C. Passive Filter Size Reduction

The pole f_c of CT and HPF was designed to be much lower than the low crossover frequency, around 30 kHz from Fig. 21, of the loop gain so that the phase is much lower than 180° at the crossover to avoid stability issues. The magnetic core part number used for CT design is ZJ42106TC from Magnetics company. It has an $A_L = 2800 \pm 20\%$ nH/Turns^2. The secondary winding has 10 turns and the wire is 24 AWG. The inductance $L_{\rm CT} = 0.23$ mH. The DM inductors $L_{\rm DM}$ and $L_{\rm DMS}$ were made with Kool-μ core from Magnetics company. The core part number for $L_{\rm DM}$ is 0077258A7 and for $L_{\rm DMS}$ it is 0077934A7. AWG 18 wire is used for both of them. $L_{\rm DM}$ has 43 turns and its inductance is 140 μH. $L_{\rm DMS}$ has 30 turns it its inductance is 71 μH. The passive filter DM capacitors and the injection capacitor $C_{\rm inj}$ are film capacitors from KEMET, rated at 275-V ac. Also, $L_{\rm DMCM}$ is 23.6 μH as given previously.

The amplifier of the active filter will be integrated as an IC and soldered on the bottom of the printed circuit board (PCB). Also, apart from the CT and the injection capacitor, all other passive components have low voltage and current ratings so it is possible to integrate them with the PCB of the original ac/dc converter. Because of these, the active filter will not contribute the converter volume significantly. In Table I, a comparison of the volumes in mm^3 of the key components in the baseline DM filter and the hybrid DM filter designed in this paper was made. From Table I, the hybrid filter of Fig. 25, can reduce the size of the baseline passive filter of Fig. 3, by around half. Fig. 28 shows the DM filter component size comparison in the experiments.

The amplifier of the active filter will be integrated as an IC and soldered on the bottom of the PCB. Also, apart from the CT and the injection capacitor, all other passive components have low voltage and current ratings so it is possible to integrate them with the PCB of the original ac/dc converter. Because of these, the active filter will not contribute the converter volume significantly. In Table I, a comparison of the volumes in mm^3 of the key components in the baseline DM filter and the hybrid DM filter designed in this paper was made. From Table I, the hybrid filter of Fig. 25, can reduce

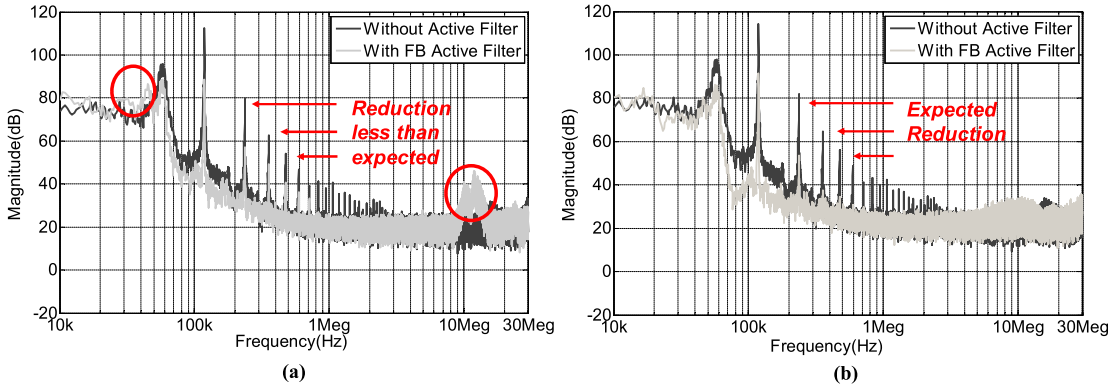

Fig. 26. DM noise Spectrum Comparison (PFC converter load 150 W) without and with the FB active filter. (a) Uncompensated unstable case. (b) Compensated stable case.

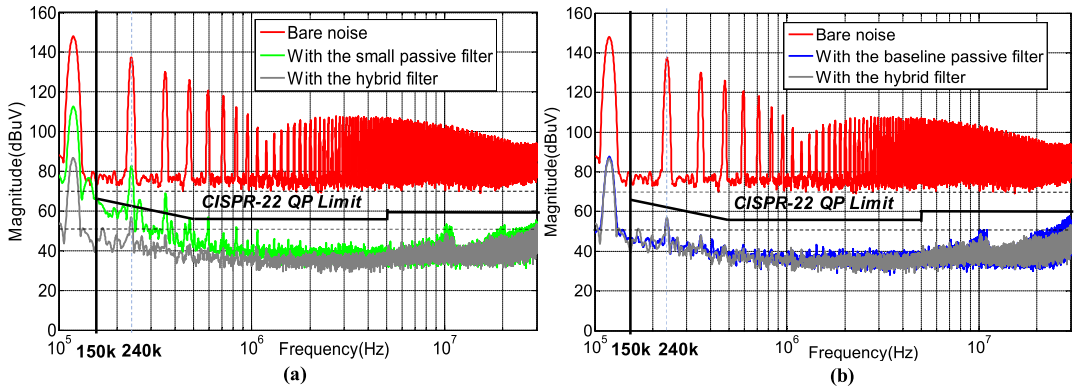

Fig. 27. DM EMI noise reduction comparison (PFC converter load 350 W). (a) Bare noise, with the small passive filter and with the hybrid filter. (b) Bare noise, with the baseline passive filter and with the hybrid filter.

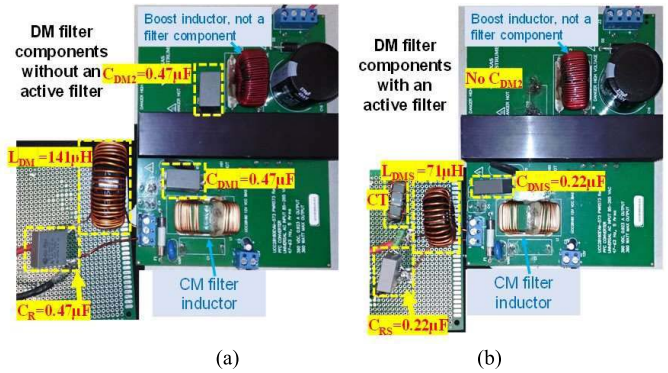

Fig. 28. Comparison of DM filter component size with and without an active filter. (a) Without an active filter. (b) With an active filter.

TABLE I

COMPARISON OF THE VOLUME OF THE KEY COMPONENTS OF THE BASELINE DM FILTER AND THE DESIGNED HYBRID DM FILTER

Baseline Filter Component Name	Volume (mm^3)	Hybrid Filter Component Name	Volume (mm^3)
DM Capacitor, C_{DM1}=0.47μF	3,762	DM Capacitor, C_{DMS}=0.22μF	1,822
DM Capacitor, C_R=0.47μF	3,762	DM Capacitor, C_{RS}=0.22μF	1,822
DM Inductor, L_{DM}=141μH	10,600	DM Inductor, L_{DMS}=71μH	4,150
DM Capacitor, C_{DM2}=0.47μF	3,762	Injection capacitor, C_{inj}=0.2μF	1,822
		CT Inductor, L_{CT}=0.23mH	1,238
Total	21,886	Total	10,854

the size of the baseline passive filter of Fig. 3, by around half. Fig. 28 shows the DM filter component size comparison in the experiments.

D. Power Dissipation

One of the big power loss contributors is 60-Hz line frequency current leaked from the injection network. For this design, C_{inj} is 0.2 μF, so the 60-Hz leakage current is around 9 mA. Because R_E and R_{inj} are small, the most significant power loss is on the transistors in class AB amplifier. It is approximately 9 mA $\times$ 15 V $=$ 135 mW.

Also, in Fig. 27, with only the small passive filter, the 120-kHz noise current is the highest at 112 dBμV and it was reduced by 30 dB or 97% after the cancellation current is injected by the active filter, so the 120-kHz current flowing through the class AB amplifier should be almost equal to the sensed 120-kHz current by CT. The 240-kHz current is 35 dB smaller than 120 kHz, so the power loss generated by 240-kHz cancellation current can be ignored. The power loss generated

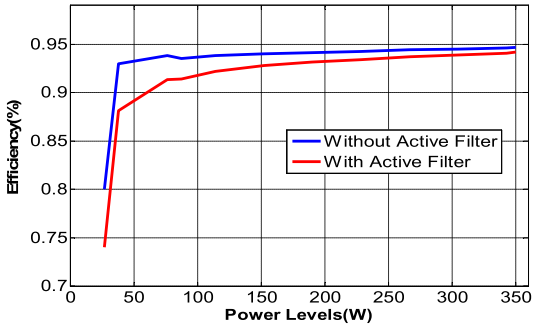

Fig. 29. Efficiency comparison of the ac/dc converter without/with the active filter.

by higher order harmonics can also be ignored since their magnitudes are even smaller than 240-kHz noise. Based on Fig. 8, when 120-kHz noise current has a 112-dBμV voltage on one LISN, the current I_R is calculated as 123 mA. So, the power loss due to 120-kHz cancellation current is 123 mA $\times$ 15 V $=$ 1.85 W. The PFC converter's DM current ripple does not change much due to the control strategy of the PFC used in the experiments, so the active filter's power loss is close to 2 W at different PFC loads. If the DM noise changes much when the PFC load changes, the power loss of the active filter should be estimated correspondingly. The power loss on auxiliary power supply is around 0.3 W. And the power loss on other small signal components is small. So, the total power dissipation in the active filter is found to be around 2.3 W which is only 0.66% of PFC converter's full power 350 W. The final measured power loss agrees with the estimated. Efficiency comparison of the ac/dc converter without/with the active filter is given in Fig. 29. Also, surge or transient suppression components should be designed between the ac power line and the active filter to make sure the filter and PFC will not be damaged in electromagnetic sensitivity tests.

VI. Conclusion

In this paper, a methodology for the analysis and design of the active filter within a hybrid DM EMI filter on the ac side of a boost PFC ac/dc converter has been presented. While most of the existing literatures focus on the analysis and design of either CM active filters or the DM active filters on the dc side, this paper focuses on a more challenging DM active filter design on the ac side. This paper developed a technique to design and model the active filter. Based on the developed model, the compensation is made to achieve stability. The developed technique and model are validated in both simulations and experiments.

References

[1] S. Wang, Y. Y. Maillet, F. Wang, D. Boroyevich, and R. Burgos, "Investigation of hybrid EMI filters for common-mode EMI suppression in a motor drive system," *IEEE Trans. Power Electron.*, vol. 25, no. 4, pp. 1034–1045, Apr. 2010.

[2] Y. C. Son and S.-K. Sul, "A new active common-mode EMI filter for PWM inverter," *IEEE Trans. Power Electron.*, vol. 18, no. 6, pp. 1309–1314, Nov. 2003.

[3] J. Biela, A. Wirthmueller, R. Waespe, M. L. Heldwein, K. Raggl, and J. W. Kolar, "Passive and active hybrid integrated EMI filters," *IEEE Trans. Power Electron.*, vol. 24, no. 5, pp. 1340–1349, May 2009.

[4] P. Pairodamonchai, S. Suwankawin, and S. Sangwongwanich, "Design and implementation of a hybrid output EMI filter for high-frequency common-mode voltage compensation in PWM inverters," *IEEE Trans. Ind. Appl.*, vol. 45, no. 5, pp. 1647–1659, Sep./Oct. 2009.

[5] Y.-C. Son and S.-K. Sul, "Generalization of active filters for EMI reduction and harmonics compensation," *IEEE Trans. Ind. Appl.*, vol. 42, no. 2, pp. 545–551, Mar. 2006.

[6] D. Hamza, M. Sawan, and P. K. Jain, "Suppression of common-mode input electromagnetic interference noise in DC-DC converters using the active filtering method," *IET Power Electron.*, vol. 4, no. 7, pp. 776–784, 2011.

[7] N. Kikuchi and T. Hirono, "The active EMI filter for suppressing common-mode noise in bridge-less PFC converter system," in *Proc. 19th Int. Conf. Electr. Mach. Syst. (ICEMS)*, Chiba, Japan, Nov. 2016, pp. 1–6.

[8] S. Takahashi, S. Ogasawara, M. Takemoto, K. Orikawa, and M. Tamate, "Common-mode voltage attenuation of an active common-mode filter in a motor drive system fed by a PWM inverter," in *Proc. 20th Int. Conf. Electr. Mach. Syst. (ICEMS)*, Sydney, NSW, Australia, Aug. 2017, pp. 1–6.

[9] D. Shin *et al.*, "Analysis and design guide of active EMI filter in a compact package for reduction of common-mode conducted emissions," *IEEE Trans. Electromagn. Compat.*, vol. 57, no. 4, pp. 660–671, Aug. 2015.

[10] M. C. Di Piazza, A. Ragusa, and G. Vitale, "Effects of common-mode active filtering in induction motor drives for electric vehicles," *IEEE Trans. Veh. Technol.*, vol. 59, no. 6, pp. 2664–2673, Jul. 2010.

[11] M. C. Di Piazza, A. Ragusa, and G. Vitale, "An optimized feedback common mode active filter for vehicular induction motor drives," *IEEE Trans. Power Electron.*, vol. 26, no. 11, pp. 3153–3162, Nov. 2011.

[12] D. Hamza, M. Qiu, and P. K. Jain, "Application and stability analysis of a novel digital active EMI filter used in a grid-tied PV microinverter module," *IEEE Trans. Power Electron.*, vol. 28, no. 6, pp. 2867–2874, Jun. 2013.

[13] W. Chen, X. Yang, and Z. Wang, "An active EMI filtering technique for improving passive filter low-frequency performance," *IEEE Trans. Electromagn. Compat.*, vol. 48, no. 1, pp. 172–177, Feb. 2006.

[14] M. C. Di Piazza, M. Luna, A. Ragusa, and G. Vitale, "An improved common mode active filter for EMI reduction in vehicular motor drives," in *Proc. IEEE Vehicle Power Propuls. Conf.*, Chicago, IL, USA, Sep. 2011, pp. 1–8.

[15] W. Chen, X. Yang, and Z. Wang, "Systematic evaluation of hybrid active EMI filter based on equivalent circuit model," in *Proc. 37th IEEE Power Electron. Specialists Conf.*, Jeju, South Korea, Jun. 2006, pp. 1–7.

[16] M. C. Di Piazza, G. Tine, and G. Vitale, "An improved active common-mode voltage compensation device for induction motor drives," *IEEE Trans. Ind. Electron.*, vol. 55, no. 4, pp. 1823–1834, Apr. 2008.

[17] W. Chen, X. Yang, and Z. Wang, "Analysis of insertion loss and impedance compatibility of hybrid EMI filter based on equivalent circuit model," *IEEE Trans. Ind. Electron.*, vol. 54, no. 4, pp. 2057–2064, Aug. 2007.

[18] W. Chen, W. Zhang, X. Yang, Z. Sheng, and Z. Wang, "An experimental study of common-and differential-mode active EMI filter compensation characteristics," *IEEE Trans. Electromagn. Compat.*, vol. 51, no. 3, pp. 683–691, Aug. 2009.

[19] A. C. Chow and D. J. Perreault, "Design and evaluation of a hybrid passive/active ripple filter with voltage injection," *IEEE Trans. Aerosp. Electron. Syst.*, vol. 39, no. 2, pp. 471–480, Apr. 2003.

[20] D.C. Hamill, "An efficient active ripple filter for use in DC-DC conversion," *IEEE Trans. Aerosp. Electron. Syst.*, vol. 32, no. 3, pp. 1077–1084, Jul. 1996.

[21] T. Farkas and M. F. Schlecht, "Viability of active EMI filters for utility applications," *IEEE Trans. Power Electron.*, vol. 9, no. 3, pp. 328–337, May 1994.

[22] R. Goswami, S. Wang, and Y. Chu, "Design of an active differential mode current filter for a boost power factor correction AC-DC converter," in *Proc. IEEE Energy Convers. Congr. Expo. (ECCE)*, Montreal, QC, Canada, Sep. 2015, pp. 4375–4382.

[23] S. Wang, F. C. Lee, and W. G. Odendaal, "Using scattering parameters to characterize EMI filters," in *Proc. IEEE 35th Annu. Power Electron. Specialists Conf. (PESC)*, vol. 1, Jun. 2004, pp. 297–303.

[24] S. Wang, F. C. Lee, and W. G. Odendaal, "Improving the performance of boost PFC EMI filters," in *Proc. 18th Annu. IEEE Appl. Power Electron. Conf. Expo.*, Miami Beach, FL, USA, vol. 1, Feb. 2003, pp. 368–374.
[25] F.-Y. Shih, Y.-T. Chen, Y.-P. Wu, and Y.-T. Chen, "A procedure for designing EMI filters for AC line applications," *IEEE Trans. Power Electron.*, vol. 11, no. 1, pp. 170–181, Jan. 1996.
[26] I. Cadirci, B. Saka, and Y. Eristiren, "Practical EMI-filter-design procedure for high-power high-frequency SMPS according to MIL-STD 461," *IEE Proc.-Elect. Power Appl.*, vol. 152, no. 4, pp. 775–782, 2005.
[27] K. Raggl, T. Nussbaumer, and J. W. Kolar, "Model based optimization of EMC input filters," in *Proc. 11th Workshop Control Modeling Power Electron.*, Zurich, Switzerland, Aug. 2008, pp. 1–6.
[28] S. Wang, F. C. Lee, and W. G. Odendaal, "Characterization, evaluation, and design of noise separator for conducted EMI noise diagnosis," *IEEE Trans. Power Electron.*, vol. 20, no. 4, pp. 974–982, Jul. 2005.
[29] S. Wang, P. Kong, and F. C. Lee, "Common mode noise reduction for boost converters using general balance technique," *IEEE Trans. Power Electron.*, vol. 22, no. 4, pp. 1410–1416, Jul. 2007.
[30] *AD829 Datasheet, AD829 IC, High Speed, Low Noise Audio OP Amp*, Analog Devices, Inc., Norwood, MA, USA, 2017.
[31] R. C. Jaeger and T. Blalock, *Microelectronic Circuit Design*, 4th ed. New York, NY, USA: McGraw-Hill, 2010, ch. 5, 15 and 17.
[32] J. Karki, "Voltage feedback vs current feedback OP amps," Texas Instrum., Dallas, TX, USA, Appl Rep. SLVA051, 1998. [Online]. Available: http://www.ti.com/lit/an/slva051/slva051.pdf
[33] Analog Devices. *MT-058: Effects of Feedback Capacitance on VFB and CFB Op Amps*. Accessed: 2017. [Online]. Available: http://www.analog.com/media/en/training-seminars/tutorials/MT-058
[34] Y. Chu, S. Wang, and Q. Wang, "Modeling and stability analysis of active/hybrid common-mode EMI filters for DC/DC power converters," *IEEE Trans. Power Electron.*, vol. 31, no. 9, pp. 6254–6263, Sep. 2016.

Rajib Goswami (S'11) received the B.Sc. Engineering M.Sc. Engineering degrees in electrical and electronic engineering from the Bangladesh University of Engineering and Technology, Dhaka, Bangladesh, in 2009 and 2012, respectively, and the Ph.D. degree in electrical engineering from the University of Texas at San Antonio, San Antonio, TX, USA, in 2017.

He served as an Electrical and Electronics Engineer with Bangladesh Atomic Energy Commission, Dhaka, from 2010 to 2012. He was a Research Intern with the PEEPRL of University of Florida, Gainesville, FL, USA. His current research interests include hybrid (active/passive) EMI filter design for DM/CM noise of power converters, EMI noise analysis and filter design for three phase converters, and power conversion from wind turbine generators (maximum power tracking).

Shuo Wang (S'03–M'06–SM'07) received the Ph.D. degree from Virginia Tech, Blacksburg, VA, USA, in 2005.

From 2005 to 2009, he was a Research Assistant Professor with Virginia Tech. From 2009 to 2010, he was a Senior Design Engineer with GE Aviation Systems, Vandalia, OH, USA. From 2010 to 2014, he was with the University of Texas at San Antonio, TX, USA, as an Assistant Professor and later as an Associate Professor. Since 2015, he has been an Associate Professor with the Department of Electrical and Computer Engineering, University of Florida, Gainesville, FL, USA. He has authored or co-authored more than 160 IEEE journal and conference papers and holds 8 U.S. patents.

Dr. Wang was a recipient of the Best Transaction Paper Award from the IEEE Power Electronics Society in 2006, two William M. Portnoy Awards for the papers published in the IEEE Industry Applications Society in 2004 and 2012, respectively, and the Prestigious National Science Foundation CAREER Award in 2012. He is currently an Associate Editor of the IEEE TRANSACTIONS ON INDUSTRY APPLICATIONS and the Technical Program Co-Chair of the IEEE 2014 International Electric Vehicle Conference.

Eugene Solodovnik received the M.S.E.E. degree (with Hons.) from the Taganrog State University of Radio-Engineering, Taganrog, Russia, in 1991, specializing in the design of control systems with variable control laws, and the Ph.D. degree in electrical engineering from the University of South Carolina, Columbia, SC, USA, in 2001, specializing in the modeling and simulation of more electric ship power systems.

He was a Research Assistant Professor with the University of South Carolina from 2001 to 2005. He joined the Boeing Company, Seattle, WA, USA, in 2005 as an Electrical Systems Design Engineer on the 787 program. He specializes in electrical power systems, power electronics, motors controllers, and energy conversion. He has authored or co-authored more than 25 papers in peer reviewed journals and conference proceedings and holds 11 patents. His current research interests include electrical power system dynamics, protections, power system modeling, and simulation and controls.

Kamiar J. Karimi (S'81–M'81) received the B.S., Master of Engineering, and Ph.D. degrees in electrical engineering from Cornell University, Ithaca, New York, in 1981, 1982, and 1986, respectively.

From 1986 to 1989, he was with Landis and Gyr Systems, San Jose, CA, USA, where he was in charge of performing research in the area of energy management systems. Since 1989, he has been with Boeing Company, Seattle, WA, USA, where he is a Senior Technical Fellow. He has led system analysis and modeling for the space station power system, power system design, power electronics research, power quality issues, and the simulation of various commercial airplane power systems including 747/767/777/787. He is one of the architects of the 787 more-electric power systems, and was the Chief Engineer for the electrical power systems from 2008 to 2011. He is leading multiple research projects related to aircraft architecture optimization, power conversion technology, and simulation of large complex dynamical systems. He is also in charge of developing energy management architectures for the next generation of Boeing Commercial Airplanes. He has authored more than 40 technical papers. He holds 20 U.S. patents in the areas of energy management, power electronics, and power system design.

Dr. Karimi is a member of SAE.